Controlling grain structure and texture in Al-Mn from the competition between precipitation and recrystallization

K. Huang [a*,b], K. Zhang[b], K. Marthinsen[b], R. E. Logé [a]

[a] Thermomechanical Metallurgy Laboratory – PX Group Chair, Ecole Polytechnique Fédérale de Lausanne (EPFL),CH-2002 Neuchâtel, Switzerland

[b] Department of Materials Science and Engineering, Norwegian University of Science and Technology, Trondheim, N-7491 Trondheim, Norway

* **Corresponding author**: Tel.: +41 21 695 44 72. E-mail address:huangke0729@hotmail.com (K.Huang)

This paper has now been formally published:

Acta Materialia

Volume 141, December 2017, Pages 360-373

https://doi.org/10.1016/j.actamat.2017.09.032

Abstract

The recrystallization behaviour of Al-Mn alloys (AA3xxx series alloys) is affected by randomly distributed dispersoids present before annealing, by dispersoids precipitated at grain/subgrain boundaries before the onset of recrystallization, and by dispersoids concurrently precipitated during recrystallization. In this study, the effects of these three populations of dispersoids on the recrystallization behaviour of a cold rolled AA3xxx alloy were analysed and compared using four temperature-time paths to different target temperatures. Changing the temperature-time path modifies the extent of recovery, the dispersoid structures, as well as the absolute recrystallization temperature, which then influences the final grain structure and recrystallization texture. In particular, an in-depth investigation on how different populations of dispersoids affect the main recrystallization texture components of AA3xxx alloys, i.e., P{011}<566>, ND-Cube {001}<310>, and Cube {001}<100>, has been carried out. The results clearly show that, as compared to isothermal annealing, annealing with more elaborate heating and annealing schedules (temperature-time paths) all lead to increased strength of the P texture component and decreased intensities of both the Cube and ND-rotated Cube texture components. The increase of P texture strength and average grain size is most significant when recrystallization occurs concurrently with precipitation. The controlling mechanisms behind this behaviour and the possibility to use them to tailor the grain structure and texture of similar alloys are further discussed.

Keywords: Precipitation; Dispersoids; Recrystallization; Crystallographic Texture; Grain boundary migration.

1. Introduction

Aluminium AA3xxx-series alloys (i.e. alloys with Mn as their main alloying element) are widely used in packaging, beverage cans and the automobile heat exchanger industry, with different requirements on grain structures and textures. The supersaturated Mn may precipitate as fine dispersoids due to its limited solubility in Al, [1], e.g., during homogenization and back annealing (i.e. annealing after cold/hot deformation), thus changing the microchemistry of the alloy in terms of solute level and particle structure [2]. Three types of dispersoids, including randomly distributed dispersoids formed during homogenization (type I), dispersoids precipitated on (sub)grain boundaries before recrystallization (type II), as well as dispersoids precipitated on (sub)grain boundaries during recrystallization (type III), are usually involved during the processing of these series of alloys. The heterogeneous precipitation of type II and III dispersoids is hence different from that found in precipitation hardening alloys such as Al-Cu where precipitation can occur homogeneously throughout the microstructure during annealing [3]. Since the grain size and texture can change significantly when the microchemistry of the material, as well as the thermo-mechanical processing conditions change [2, 4], there is a strong scientific and industrial interest in better understanding and controlling the combined effect of these three types of dispersoids on recrystallization of the non-heat treatable Al 3xxx alloy products.

The fine dispersoids precipitated out during homogenization after casting (type I) are mainly randomly distributed and their effect on the subsequent recrystallization behaviour after deformation is relatively well understood. The effect of this type of dispersoids has often been analysed by annealing the deformed materials at high temperature to avoid the other two types (type II and III) of dispersoids. This usually leads to an equiaxed grain structure with Cube as the major texture component [2, 5].

Cold or hot deformation after homogenization introduces more heterogeneous nucleation sites for precipitation. At low annealing temperatures of the deformed material, dispersoids can heterogeneously precipitate on grain/subgrain boundaries before possible recrystallization initiates (type II) or concurrently with recrystallization (type III) [4-6]. The precipitation of large numbers of type II and/or III dispersoids at lower annealing temperatures can retard or even totally suppress recrystallization [5-7]. In addition to slow recrystallization kinetics and a resulting coarse elongated grain structures, less common texture components like ND-rotated cube {001}<310> and P {011}<566> are often observed when precipitation occurs during annealing [2, 4-6, 8-13]. The effect of dispersoids of type II and III on the development of the P-orientation is usually not separately investigated, since they are collectively considered as "concurrent precipitation". The individual contribution from type II and type III dispersoids therefore requires further investigation.

Annealing with different temperature-time paths modifies the microchemistry evolution, it can thus determine which type of dispersoids interacts with recrystallization, an aspect which has not been systematically investigated so far. Cold-rolled AA3xxx-type alloy specimens were annealed by Schäfer and Gottstein [14] using different temperature-time paths, however, the effect of dispersoids along grain/subgrain boundaries before recrystallization (type II) was mostly left unexploited. In another recent work, the effect of type II dispersoids on the recrystallization behaviour of an *as-cast* AA3xxx model alloy, which has negligible type I dispersoids, was investigated [15]. However, annealing of the deformed as-cast AA3xxx alloys leads to a less frequently observed sharp M {113}<110> component [4, 12, 15], which shares some similarities with, but which is still distinctively different from the P- and ND-rotated cube texture components and makes the analysis more complex. The influence of "concurrent

precipitation" (both type II and III according to the current definition) on the recrystallization behaviour of the same material has recently been *quantitatively* investigated in terms of nucleation and growth behaviour of the P-orientation [16]. Computer simulations have also been performed to study and probe the complex interactions between dispersoids and recrystallization. In these conditions, physically based numerical models usually fail to predict the correct recrystallization kinetics [7, 17]. The different grain structures and recrystallization textures obtained at different annealing temperatures are usually not described, see e.g. Refs [18, 19]. In other words, there is currently no numerical model that can successfully predict the different grain structures and recrystallization textures during annealing with different temperature-time paths of cold deformed AA3xxx alloys. To the best knowledge of the authors, there is no detailed analysis focusing on the combined effect of these three populations of dispersoids on recrystallization, even though each of them, to a different extent, does play a role in determining the recrystallization kinetics, final grain structure and texture.

In this study, a homogenized AA3xxx model alloy, which contains a large number of randomly distributed fine dispersoids, was cold rolled to a true strain of ε=3.0. These deformed samples were then heated with four carefully designed temperature-time schedules to various target temperatures to induce dispersoid precipitation preferentially located at grain/subgrain boundaries, before and during recrystallization, respectively. The main objective is to explore the effect of these three different populations of dispersoids on the microstructure and crystallographic texture of the AA3xxx alloy. The results obtained in this paper provide new understanding for microstructure design through thermo-mechanical processing of particle-containing metallic materials, as well as a guide to its associated numerical modelling. The

different temperature-time paths are expected to have limited effect on the variation of large constituent particles at the investigated target temperatures [20, 21].

2. Experimental

The examined material was a DC-cast AA3xxx-type model alloy supplied by Hydro Aluminium, with the chemical composition (wt.%) of 0.152% Si, 0.530% Fe, 0.390% Mn. Previous experiments have shown that about 0.35 wt % of Mn is still in solid solution after casting, the other small part was precipitated out as large constituent particles of ~0.88 μm in diameter [2]. The as-cast material was homogenized in an air circulation furnace where the samples were heated at 50°C/h from room temperature to 450°C and then kept for another 4 hours before water quenching. It has previously been shown that in this condition 0.16 wt % of Mn was still left in solid solution [2], i.e., 0.19 wt % of Mn was consumed either such as to produce randomly distributed fine dispersoids with average diameter of 50 nm and number density of 1.3×10^6 mm^{-2} (particles smaller than 20 nm are not counted), or contribute to the growth of constituent particles which reached about 0.96 μm in diameter.

The homogenized materials were cold rolled with good lubrication conditions at room temperature from slabs of a thickness of 30 mm to 1.5 mm by multiple passes to an accumulated true strain of $\varepsilon = 3.0$. The rolled sheet was water cooled after few passes to avoid deformation heating. These deformed samples were then annealed according to the four different temperature-time paths illustrated in Fig.1. One set of the deformed samples were directly annealed in a pre-heated salt bath at: i) 500^{o}C for 5s; ii) 350^{o}C for 10^5s and iii) 400 ^{o}C for 10^5s, all referred to as isothermal annealing samples as shown in Fig.1a. Another set of samples were subjected to a two-step annealing where the samples were isothermally pre-annealed at 300^{o}C for

10^4s before the final annealing at 350, 400 and 500 ^{o}C, respectively, as shown in Fig.1b. The samples subjected to three-step annealing, as shown in Fig.1c, were heated at 50°C/h to 300°C and held for 10^4s before the final isothermal annealing step. In addition, some samples were annealed with a constant heating rate of 50°C/h all the way to the target temperatures, followed by isothermal annealing for 10^5s, as illustrated in Fig.1d, hereafter just termed as "slow annealing". Finally, a few supplementary tests slowly annealed to 325°C and 335°C, which will be detailed later in the discussion part when relevant results appear, were also conducted. All samples were quickly water quenched after the heat treatments.

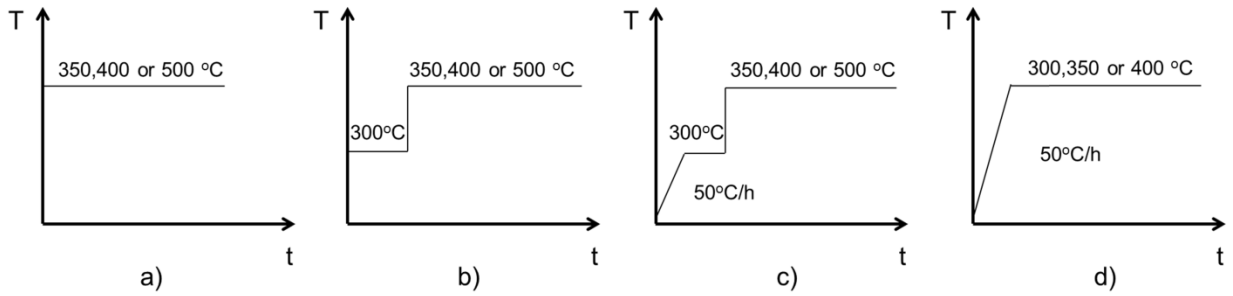

Fig. 1 Schematic graph showing the four temperature-time paths used during annealing

a) Isothermal annealing; b) two-step annealing; c) three-step annealing; d) slow annealing.

The evolution of electrical conductivity (EC) was measured in order to estimate the precipitation behaviour, with eight measurements conducted on the rolling direction (RD) - transverse direction (TD) section for each condition, even though only the averaged values and associated standard deviations are shown in this work. The RD- normal direction (ND) cross sections of the samples were polished according to standard metallographic procedures. Particles were observed with a backscattered electron (BSE) detector and grain structure and orientation were obtained by Electron backscatter diffraction (EBSD) in a Zeiss Supra 55 or FEI XLF 30

field emission gun scanning electron microscope (FEG-SEM), at the Norwegian University of Science and Technology (NTNU) and Ecole Polytechnique Fédérale de Lausanne (EPFL), respectively. Inverse pole figure (IPF) maps of the annealed samples were obtained and analysed with the TSL or HKL softwares, using a scanning step size of 0.25-2 μm, to study both the grain structure and recrystallization texture. In all micrographs, the horizontal direction corresponds to the RD direction while the vertical direction is the ND direction. Due to the large grain size in most of the investigated conditions, a large area (~2-4 mm^2) was scanned by EBSD to give a statistically reliable representation of the texture and average grain size, although only a small area is usually presented in the micrograph. The grain size was measured as the equivalent circular diameter in the RD-ND cross section. The texture measured by EBSD was represented through orientation distribution functions (ODFs) by imposing orthotropic symmetry, and using the harmonic series expansion method (L=22) and a Gaussian half-width of 5°. In this work, the volume fractions of {001}<100> (Cube), {011}<566> (P) and {001}<310> (ND-rotated cube) texture components were quantified using EBSD orientation maps. Unless otherwise specified, a grain is classified as belonging to a specific texture component if it is within a 15° scatter from the ideal component when calculating the fractions of the three texture components.

3. Results

3.1 Recrystallization and precipitation kinetics

The four different temperature-time paths in Fig. 1 are actually composed of several isothermal annealing and/or slow annealing steps. The recrystallization and precipitation kinetics during isothermal annealing and slow annealing are now examined (Fig. 1a and d, respectively). It can be seen from Fig.2a that recrystallization finishes after annealing for 5s at 500°C, while 10^5s was not enough to complete recrystallization at 300°C. During isothermal annealing, precipitation increases in general with annealing time at all temperatures, but it is clear that the completion of recrystallization slows down the precipitation kinetics, as can be seen in Fig.2b. While precipitation kinetics can be accelerated at higher annealing temperatures due to a faster diffusion rate, it could also be retarded due to lower precipitation potential associated with the higher solubility of alloying elements (in particular Mn). During slow annealing at 50°C/h, recrystallization started at ~325°C and completed at ~350°C, while precipitation kept increasing with increasing temperature, even though the rate of increase clearly slowed down from 350°C to 400°C (see Fig.2c). The choice of annealing temperature and time at the intermediate annealing step in Figs. 1b and c was made according to Fig.2, such that no significant recrystallization is initiated yet while additional fine dispersoids have precipitated along grain/subgrain boundaries (type II).

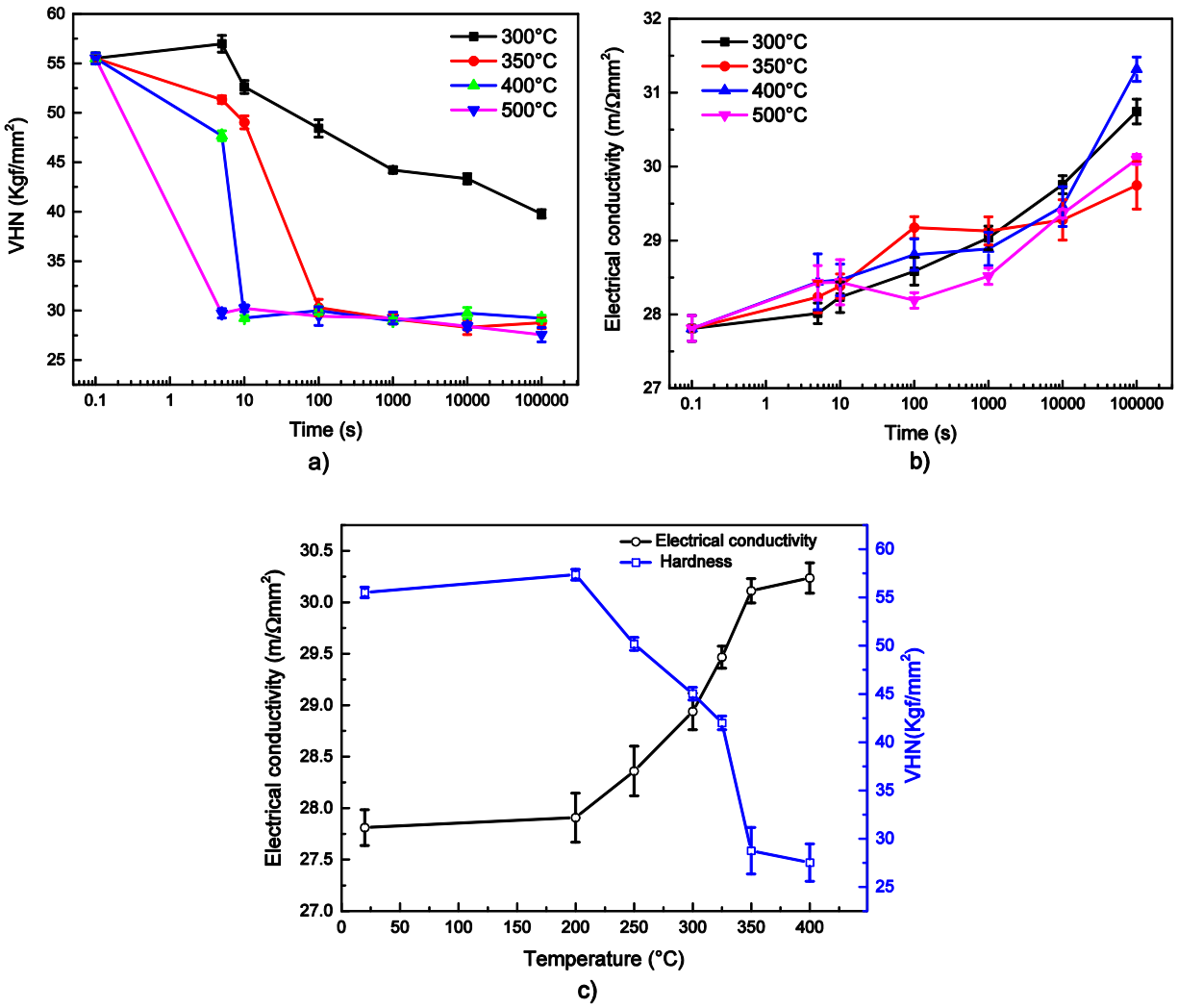

Fig.2 Recrystallization and precipitation kinetics during annealing of deformed samples (ε=3.0).

a) Hardness evolution during isothermal annealing; b) Electrical conductivity evolution during isothermal annealing; c) Hardness and electrical conductivity evolution during annealing at 50°C/h from room temperature to 400°C without holding time

The microstructure and pre-existing dispersoids (type I, ~50nm) after deformation are shown in Fig.3a, where it can be seen that the pre-existing dispersoids are mainly randomly distributed, with many of them located in the subgrain interior as indicated by black arrows (Fig.3b), the subgrains being clearly elongated along the RD direction. The EC value after deformation before annealing is 27.8 m/Ωmm2, and it increased to 28.9 m/Ωmm^2 when the sample was heated at

50°C/h to 300°C without any holding time. This is an indication that dispersoids have been precipitated out before the final annealing step for the conditions in Fig.1b and Fig.1c. One may argue that the increase of EC value could be solely due to the coarsening of existing particles, instead of the precipitation of type II dispersoids. However, quantitative measurement using BSE micrographs (all visible particles were counted) indicated that the number density of fine dispersoids indeed increased by 27% when the deformed sample (Fig.3a) was heated at 50°C/h to 300°C (Fig. 3b). In Figs.3c and d, the sample is heated at 50^{o}C/h to 300 ^{o}C (without any holding time), and finer dispersoids which most probably were precipitated out during this heating process are indicated by black arrows. The subgrain growth during this process is also clear, the strongly elongated subgrains along RD have now clearly also extended in the ND direction. Some of the subgrains are almost equiaxed, but remaining elongated subgrains still exist, as can be seen in Fig.3d. Isothermal annealing of the sample at 300°C for 10^5s leads to an electrical conductivity (EC) of 30.5 m/Ωmm^2, while this value is 31.3 m/Ωmm^2 if slow annealing (see Fig.1d) is used, i.e., indicating more dispersoids being precipitated out during slow annealing. The same tendency was observed when comparing samples after isothermal annealing and slow annealing at 300°C for 10^4s. The EC values for the samples in these different conditions, which reflect the global precipitation behaviour, are given in Table 1.

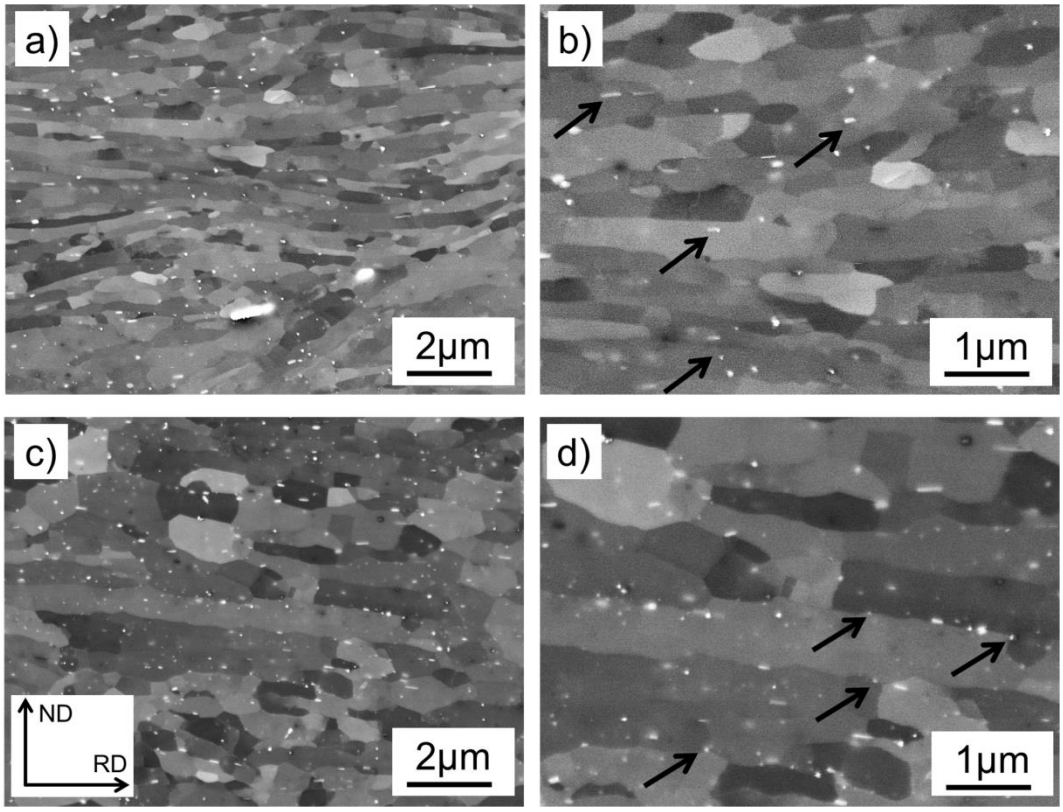

Fig.3 BSE images to show the microstructure of the cold rolled specimens (ε=3.0) before and after annealing in different conditions. a) After deformation to 3.0, showing the randomly distributed pre-existing dispersoids and elongated subgrain boundaries; b) An enlarged area from a) to show type I dispersoids; c) 50°C/h to 300°C, showing the well-defined subgrain structure and additionally precipitated fine dispersoids; d) An enlarged area from c) to show the potentail type II dispersoids.

Table 1 List of the electrical conductivity (EC) values in different conditions

Conditions		EC ($m/\Omega mm^2$)
Deformed sample		27.8 ± 0.2
Isothermal annealing	300°C@10^4s	29.6 ± 0.1
	300°C@10^5s	30.5 ± 0.2
Slow annealing (50°C/h from room temperature)	300°C@0s	28.9 ± 0.2
	325°C@0s	29.4 ± 0.1
	335°C@0s	29.6 ± 0.1
	300°C@10^4s	29.9 ± 0.1
	300°C@10^5s	31.3 ± 0.2

Note: Isothermal annealing at 300°C@10^4s is equivalent to the first step of the two-step annealing and slow annealing at 300°C@10^4s is equivalent to the first two steps of the three-step annealing. Recrystallization starts around 325°C during slow annealing with heating rate of 50°C/h.

During slow annealing (see Fig.2c), Type II dispersoids were precipitated on (sub)grain boundaries when heating the sample at 50°C/h up to ~325°C (recrystallization starts at about 325°C and finishes at about 350°C) and type III dispersoids were concurrently precipitated out during annealing between 325°C to 350°C. Since recrystallization in particle-containing Al alloys is quite heterogeneous, local variations in (sub)grain orientation and dispersoids structure are also important. In this regard, areas of interest were examined by both BSE micrographs and EBSD maps, as the former gives the dispersoid structure and their spatial distribution, whereas the latter provides crystallographic orientations maps.

3.2 Annealing at 500°C with different temperature-time paths

The separate effect of randomly distributed dispersoids (type I) obtained during homogenization was studied by annealing the deformed samples at high temperature. In the first treatment, the deformed samples were annealed at 500^{o}C for 5s (Fig.4a), during which the other two populations of dispersoids were kept at limited levels. Another deformed sample was subjected to a two-step annealing to the final temperature of 500°C, where some additional dispersoids (type II) were precipitated out along grain/subgrain boundaries before the final step at 500°C for 5s (cf. Fig. 1b). As shown in Fig.4b, the recrystallized grain size for the two-step annealed sample is obviously much larger than that of the isothermally annealed sample (Fig.4a). The average grain size of the three-step annealed sample (Fig. 4c) is actually smaller than the two-step annealed one (Fig.4b), as can be seen from Table 2. The slow annealing was not performed at 500°C, since recrystallization is complete before reaching 500°C [4]. The reason for the different grain structures will be detailed later in the discussion section.

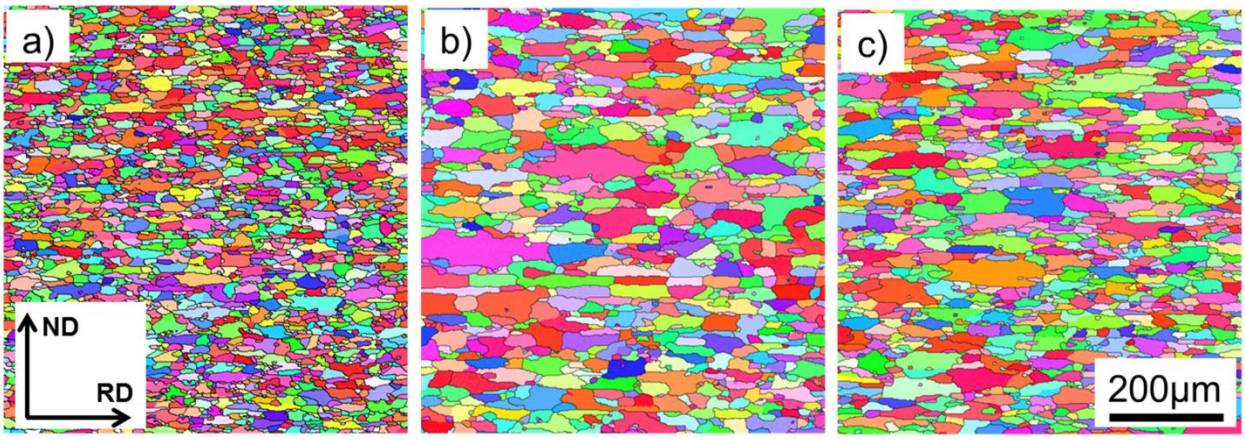

Fig.4 EBSD maps (TSL software) to show the recrystallized microstructure after annealing with different temperature-time paths. a) Isothermal annealing at 500^{o}C for 5s; b) Two-step annealing at 500^{o}C for 5s; c) Three-step annealing at 500^{o}C for 5s.

Table 2 The volume fraction of typical recrystallization texture components annealed with different temperature-time path to 500^{o}C for 5s, together with maximum texture intensities for all orientations in ODF and the average recrystallized grain size

	Cube (%)	ND-Cube (%)	P (%)	Max. texture intensity (times random, R)	Average gain size (μm)
Isothermal annealing	7.9	11.9	8.3	6.9	22.3
Two-step annealing	4.6	10.1	12.0	4.6	42.4
Three-step annealing	4.5	10.7	12.1	5.0	34.0

Recrystallization textures were measured by EBSD such that it is straightforward to quantify the volume fractions of different texture components by the TSL software. Fig.5 shows the final recrystallization textures of the samples annealed with the three different temperature-time paths corresponding to the grain structures illustrated in Fig.4. In all three cases, weak recrystallization textures were obtained. The dominating recrystallization texture components are the Cube, P and ND-rotated cube texture components (their positions in the section of $\varphi_2 = 0°$ are schematically shown in Fig.5d), for which their volume fractions are listed in Table 2. As compared to the case of isothermal annealing, there is a slight decrease in the volume fraction of the Cube and ND-rotated cube texture components, while the intensities of the P texture component clearly increased for the two- and three-step annealing.

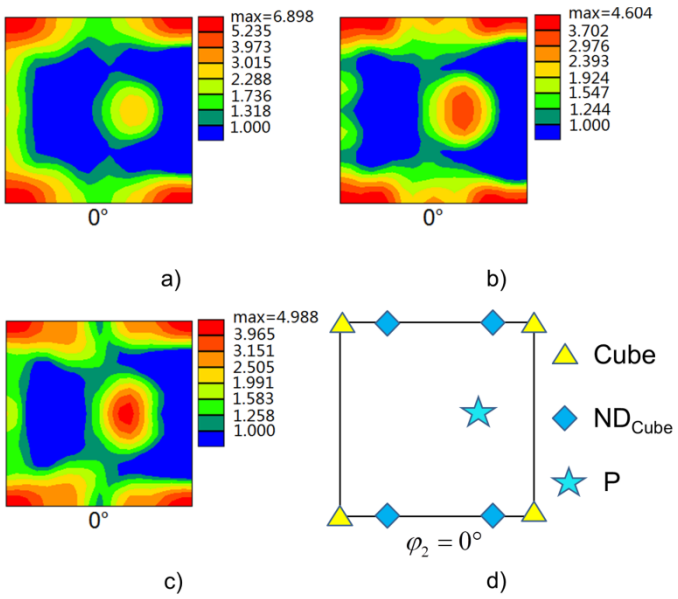

Fig.5 ODF maps (TSL software) of φ_2 =0° to show the recrystallization textures after annealing with different temperature-time paths. a) Isothermal annealing at 500°C for 5 s; b) Two-step annealing at 500°C for 5 s; c) Three-step annealing at 500°C for 5 s; d) Position of typical texture components in the section of $\varphi_2 = 0°$

3.3 Annealing at 400°C with different temperature-time paths

The deformed samples were also annealed at temperatures where recrystallization and precipitation take place simultaneously, i.e., with concurrent precipitation. The grain structures of the samples heated with four different temperature-time paths to 400°C and then kept for 10^5s are shown in Fig.6. At 400°C, recrystallization starts immediately once the sample is immersed into the pre-heated salt bath and is completed within 10s during isothermal annealing [2], i.e., there is limited precipitation of dispersoids along grain/subgrain boundaries (type II) before the onset of recrystallization during isothermal annealing in Fig.6a. The two-step and three-step annealed samples exhibited larger grain sizes as compared to the isothermally annealed one. A significant increase in grain size was obtained for the slow-annealed sample, with an elongated grain structure (pan-cake shaped grain structure). The corresponding textures in the form of

ODFs (φ_2 section) are shown in Fig. 7, and the volume fraction and maxima of the main components are given in Table 3 together with the average grain sizes.

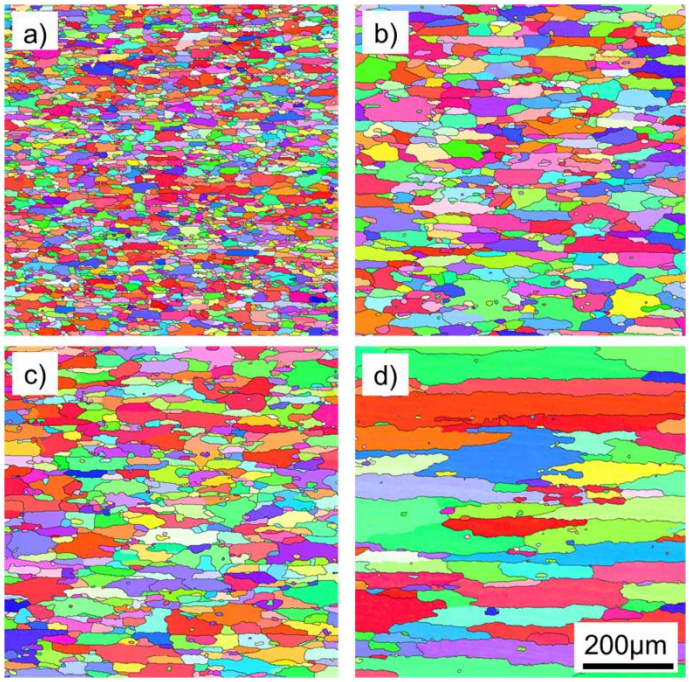

Fig.6 EBSD maps (TSL software) to show the recrystallized microstructure after annealing with different temperature-time paths. a) Isothermal annealing at 400°C for 10^5s; b) Two-step annealing at 400°C for 10^5s; c) Three-step annealing at 400°C for 10^5s; d) Slow annealing at 400°C for 10^5s.

For the isothermally annealed sample, Cube and ND-rotated cube are the major texture components, while the P-texture is fairly weak, as shown in Fig.7a. The maximum recrystallization texture intensities, as well as the volume fraction of the major texture components, remain more or less the same for the two-step and three-step annealed samples, as can be seen in Fig.7b and Fig.7c, and Table 3. As compared to the *isothermally annealed case*, the P orientation has now become the strongest texture component while the volume fractions of the Cube and ND-rotated cube components decreased only by 0.8% and 2.6%, respectively. The strengthening of the P texture component is most significant for the slow-annealed sample, where its volume fraction reaches a value as high as 46% (i.e. an increase of 39% as compared to

its isothermal counterpart). The increased volume fraction of the P-orientation must come from the consumption of orientations other than Cube and ND-rotated cube.

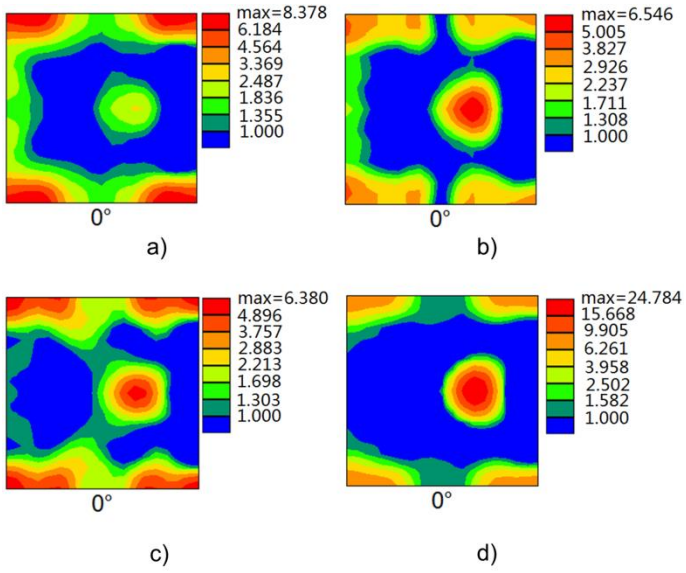

Fig.7 ODF maps (TSL software) of φ_2 =0° to show the recrystallization textures after annealing with different temperature-time paths.

a) Isothermal annealing at 400°C for 10^5s; b) Two-step annealing at 400°C for 10^5s;

c) Three-step annealing at 400°C for 10^5s; d) Slow annealing at 400°C for 10^5s.

Table 3 The volume fraction of typical recrystallization texture components annealed with different temperature-time path to 400°C for 10^5s, together with maximum texture intensities in ODF and the average recrystallized grain size

	Cube (%)	ND-Cube (%)	P (%)	Max. texture intensity (times random, R)	Average gain size (μm)
Isothermal annealing	7.7	14.0	7.2	8.4	24.2
Two-step annealing	4.8	9.1	14.6	6.5	55.0
Three-step annealing	5.1	11.3	12.7	6.4	50.3
Slow annealing	6.9	11.4	46.2	24.8	159.8

3.4 Annealing at 350°C with different temperature-time paths

The target annealing temperature for the final step was further decreased to 350^{o}C since it is well documented that the P and ND-rotated cube texture components are favoured at lower temperatures [2, 5]. At the low annealing temperature of 350°C, recrystallization started after ~5s (see Fig.2a), a fine grain structure can still be observed after isothermal annealing as shown in Fig.8a. The elongated grain structure is more obvious for the other three cases with more elaborate heating schedules (see Figs.8b-d). There is no notable difference in terms of grain structure and average grain size for the two- and three-step annealed samples. As shown in Fig.8d, the largest recrystallized grain size is found for the slow annealed sample where all three populations of dispersoids are involved.

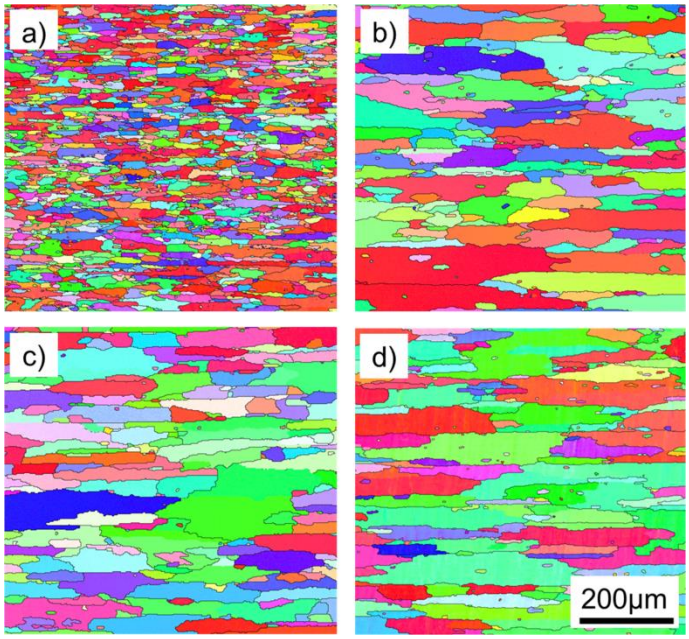

Fig.8 EBSD maps (TSL software) to show the recrystallized microstructure after annealing of the deformed samples with three different temperature-time paths. a) Isothermal annealing at 350^{o}C for 10^{5}s; b) Two-step annealing at 350^{o}C for 10^{5}s; c) Three-step annealing at 350^{o}C for 10^{5}s; d) Non-isothermal annealing at 350°C for 10^{5}s.

As shown in Fig.9, the recrystallization texture after annealing at 350°C with different heating paths can again be characterized by the P-, Cube- and ND-rotated cube texture components, i.e. those commonly observed for recrystallized AA3xxx alloys. However, as compared to the former two cases annealed at higher temperatures, generally stronger recrystallization textures were obtained at 350^{o}C. The volume fraction of the P-texture component increased to ~11% (see Table 4) after isothermal annealing, even though it is not yet the strongest texture component. In the two- and three-step annealed samples, the volume fractions of the P-texture component, which now becomes the main texture component (as listed in Table 4), are quite close, both being higher than that of the isothermally annealed sample. It is worth mentioning that the ND-rotated cube texture component is apparently the strongest texture component in Fig. 9b, even though quantitative measurements have shown that the P-texture component is actually the strongest one. This is due to the fact that ND-rotated cube overlaps with the Cube component in the ODF maps. For the slowly annealed sample, the P-texture intensity is much stronger, as shown in Fig.9d. It is actually not further strengthened when decreasing the target temperature from 400°C to 350°C during slow annealing, as can be noticed by comparing the relevant volume fraction values in Table 3 and Table 4. This is because recrystallization is actually completed when the temperature reaches 350°C during slow heating [4], and only additional grain growth accounts for the further minor texture change.

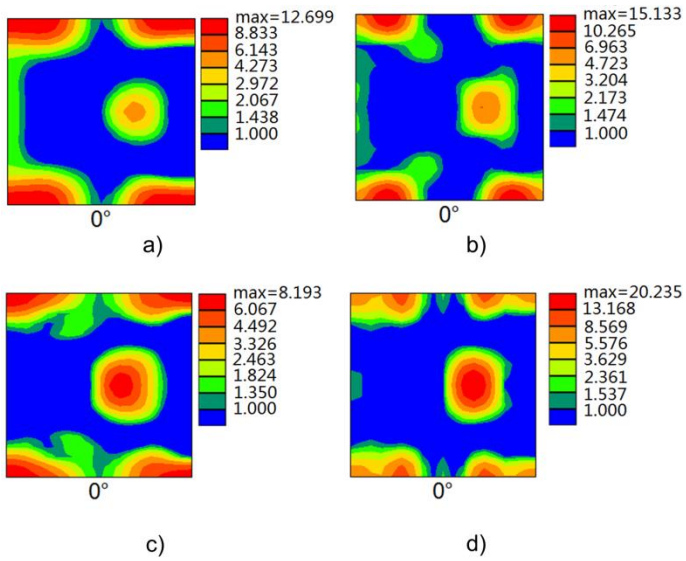

Fig.9 ODF maps (TSL software) to show the recrystallization textures after annealing of the deformed samples with four different temperature-time paths. a) Isothermal annealing; b) Two-step annealing; c) three-step annealing; d) Slow annealing

Table 4 The volume fraction of typical recrystallization texture components annealed with different temperature-time path to 350°C for 10^5s, together with maximum texture intensities in ODF and the average recrystallized grain size

	Cube (%)	ND-Cube (%)	P (%)	Max. texture intensity (times random, R)	Average gain size (μm)
Isothermal annealing	9.8	23.1	11.6	12.7	45.7
Two-step annealing	5.7	19.1	21.2	15.1	104.0
Three-step annealing	7.8	11.1	20.0	8.2	98.0
Slow annealing	4.9	16.6	41.8	20.2	171.0

4. Discussion

In this study, a homogenized material with a significant amount of fine randomly distributed dispersoids were cold rolled at room temperature by multiple passes to an accumulated deformation strain of $\varepsilon = 3.0$. The samples were subsequently annealed through four different temperature-time paths to further modify the dispersoid structures (i.e. introducing additional populations of dispersoids), and the recrystallized grain structure and texture were then carefully analysed.

4.1 Different grain structures

The microstructures after isothermal annealing are always finer and less elongated as compared to those annealed through other temperature-time paths, as shown in Figs.4, 6 and 8. Under isothermal annealing at 350°C, recrystallization started quickly at ~5s before considerable type II precipitation occurred, nucleation of recrystallization is thus not significantly suppressed. Moreover, recrystallization could complete within 100s before substantial type III dispersoids took place, leading to fine and only slightly elongated grain structures. The situation is even more so for samples isothermally annealed at higher temperatures, recrystallization is complete before any significant precipitation occurs at 500°C.

For the step and slow annealed samples, considerable type II dispersoids, which suppresses nucleation of recrystallization, were heterogeneously precipitated on (sub)grain boundaries before the onset of recrystallization. Much less recrystallized grains were formed as compared to the isothermally annealed cases. The growth of these few recrystallized grains was further influenced by pinning effects from concurrent precipitation (i.e. type III dispersoids). Because the grain and subgrain structures (Fig.3a) after cold rolling were pan-cake shaped with the

smallest dimension along ND, lamellar alignment of type II dispersoids were precipitated along some of these boundaries during low temperature annealing since boundary diffusion has a lower activation energy than lattice diffusion [6]. These subgrains, which are pinned by precipitated dispersoids, keep their elongated shape before the onset of recrystallization. However, subgrains with very limited disperoids precipitated on their boundaries can grow into equiaxed shape during annealing, as show in Fig.3c. During recrystallization, the growing grains still experience the largest pinning effect in the ND direction due to the existence of some elongated subgrains with dispersoids (both types II and III) aligned along their boundaries, which then results in an elongated grain structure thus result. The elongated grain structure after slow annealing is in agreement with literature [5, 6], where similar alloys were investigated. It is worth noticing that other affecting factors may also contribute to the elongated grain structure after slow annealing, which will be further discussed in Section 4.4.

It appears from Tables 2-4 that the grain sizes of the two-step annealed samples are always slightly larger than that of the three-step annealed samples. The microstructures of the two-step and three-step samples are thus further examined *before* the start of their final annealing step (500°C for 5s). Existing EBSD maps with large step size of 1.0 μm show no clear indication of recrystallization for either of these two conditions, higher magnification EBSD maps with finer step size of 0.3 μm were thus scanned to analyse potential nuclei, as shown in Fig.10. The microstructures of the two conditions (see Figs.10a and b) are globally quite similar, and this is also true for the misorientation distributions (Fig.10c). A careful characterization of potential nucleus has been conducted where a crystal is considered as a potential recrystallization nuclei if: i) it is larger than 7 times the step size (i.e., 2.1 μm [8]); ii) it has an interior average misorientation less than 0.5°; and iii) it is at least partially surrounded by high angle grain

boundaries. Quantitative characterization with these criteria (in the same area of 120×90 μm^2) shows that there are 54 and 66 potential nuclei for the two-step annealing and three-step annealing, respectively. This difference is because the longer annealing time for the three-step annealing strengthens static recovery and provides more subgrain growth (see Fig.10d). This increased nucleation potential can be sufficient to offset the drop of driving force, leading to a *slightly* smaller recrystallized grain size. Similar phenomena have been reported by Brechet and co-workers [22, 23], as well as by others on a similar AA3xxx alloy [24].

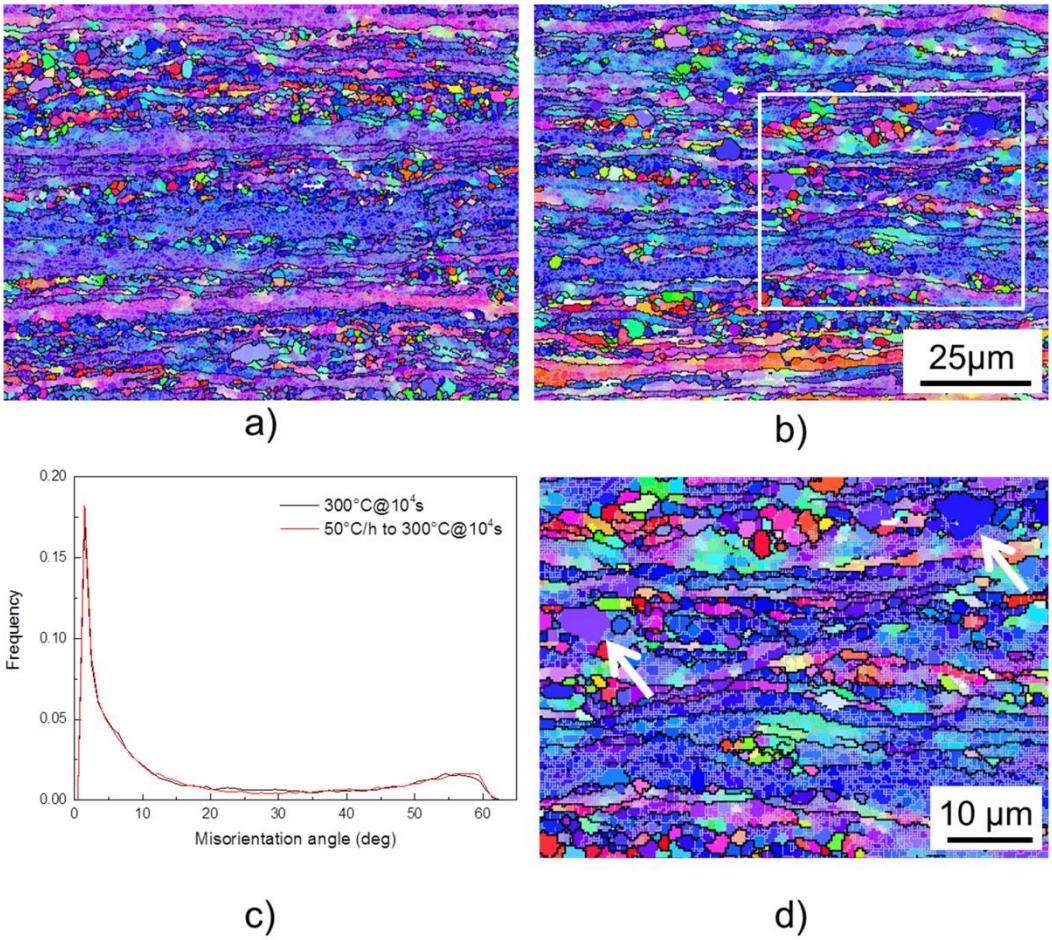

Fig.10 EBSD maps (step size 0.3μm, same area of 120×90 μm^2, HKL software) to show the microstructure before the last step of two- and three-step annealing: a) Isothermal annealing to 300°C@10^{4}s; b) slow annealing to 300°C@10^{4}s; c) Misorientation angle disribution; d) enlarged area of the white box in b).

In terms of recrystallization texture, the difference is most significant for the P-orientation (see Figs. 5, 7 and 9). The following discussion is therefore focused on this specific texture component, particularly in cases where an elongated coarse grain structure was observed.

4.2 Existing explanations to a strong P texture

The formation of strong recrystallization textures is usually explained through the oriented nucleation and/or oriented growth theory, and the P-texture should not be an exception. It has been confirmed by EBSD [4, 5, 14, 25, 26], TEM [27, 28] and numerical simulations [29-31] that P-oriented grains/sub-grains already exist within the deformation zone around constituent particles after large rolling deformations. Our previous experimental work focusing on the same alloy also confirmed this [4].

Even though the origin of P-oriented grains is now widely accepted, their further development during annealing has not been well documented. It has also been *assumed* that P-oriented grains are more likely to grow out of the deformation zone into the deformed matrix due to their close to 40°<111> special grain boundary relationship [4, 5, 8, 14, 25, 31], i.e. a boundary with reduced energy, and with a migration rate faster than general high angle grain boundaries [32]. However, direct experimental evidence of this special grain boundary relationship is rare even though it is noted that the growth advantage of other orientations with similar orientation relationship with deformed matrix is reported [32, 33]. It has also been found that large grains (not P-grains in particular), recrystallized during annealing after cold rolling of high-purity aluminium, indeed have a close to 40°<111> relationship to the deformed matrix, although full evidence requires 3-D data, and the morphology of the deformed microstructure and local variations in stored energy may also play a significant role [34]. This lack of

documentation of the growth behaviour of the coarse elongated P-grains is due to at least three aspects. Firstly, the number fraction of P-grains is generally fairly low even in conditions favouring a strong P-texture, so the probability that nuclei of P-orientation will be evidenced if a small area is followed by in-situ annealing experiments using TEM or EBSD is limited. Secondly, the boundaries between P-grains and the deformed matrix change during growth, i.e. the nature of P-grain boundaries change with the orientation of their adjacent deformed matrix. The thickness of the laminated deformed grains along ND is less than 10 μm after a true strain of 3.0, this means the large P-grains (with thickness of >100 μm) which are growing along RD can simultaneously be exposed to several deformed grains of different orientations. The fast growing sections can quickly consume the laminated grains with which they have approximately a 40°<111> orientation relationship, leading to a lost of evidence. However, numerically rotating all the experimentally measured orientations of the deformed matrix of the same alloy by 38° around the 8 possible <111> axes (Σ7) leads to an evident P component [4]. This indicates that some of the existing P-nuclei around large particles, which are experimentally verified, will have a close to 40°<111> special orientation relationship with the deformed matrix during their growth and thus benefit from a *growth advantage*.

These ‘theories’ imply that large P-grains should prevail in all conditions, as long as they pre-exist in the deformed matrix and have a close to 40°<111> special orientation with the matrix. However, the results presented in this paper clearly showed that the strength of P-texture is not always the highest when the temperature-time paths change, even though the same starting material is used, i.e., with the same orientation relationship between P-grains and deformed matrix.

4.3 Conditions for a strong P texture

Recrystallization completes very quickly during isothermal annealing at high temperatures due to the large cold deformation (ε=3.0), so precipitation before and during recrystallization, i.e., type II and III dispersoids, *during isothermal annealing* exist but their effect is very weak and is neglected for qualitative analyses. During isothermal annealing at high temperatures, where type I dispersoids acts mostly alone, P-texture is never the strongest texture component (see Fig.5a and Fig.7a) and elongated coarse grain structures are usually not observed (see Fig.4a and Fig.6a). However, it does not necessarily mean that P-texture will be weak for all cases during isothermal annealing. When the sample was isothermally annealed at the lower temperature of 325°C (see Fig.11a), the P-texture still becomes the dominant component even though it is still weaker than its slowly annealed counterpart, as can be seen in Fig.12 and Table 5. The strongly elongated coarser P-grains can be easily seen in Fig.11c. Since the incubation time of recrystallization is still relatively short (~10s), the precipitation during annealing before recrystallization (type II) is limited and not held responsible for the dominant P-texture during isothermal annealing at 325°C. It is worth mentioning that low annealing temperature in itself does not guarantee a strong P-texture in this material. It has been shown that annealing the same material, but with limited type II and III dispersoids (resulting from different prior homogenization procedures), does not lead to a dominant P-texture even at 300°C [2].

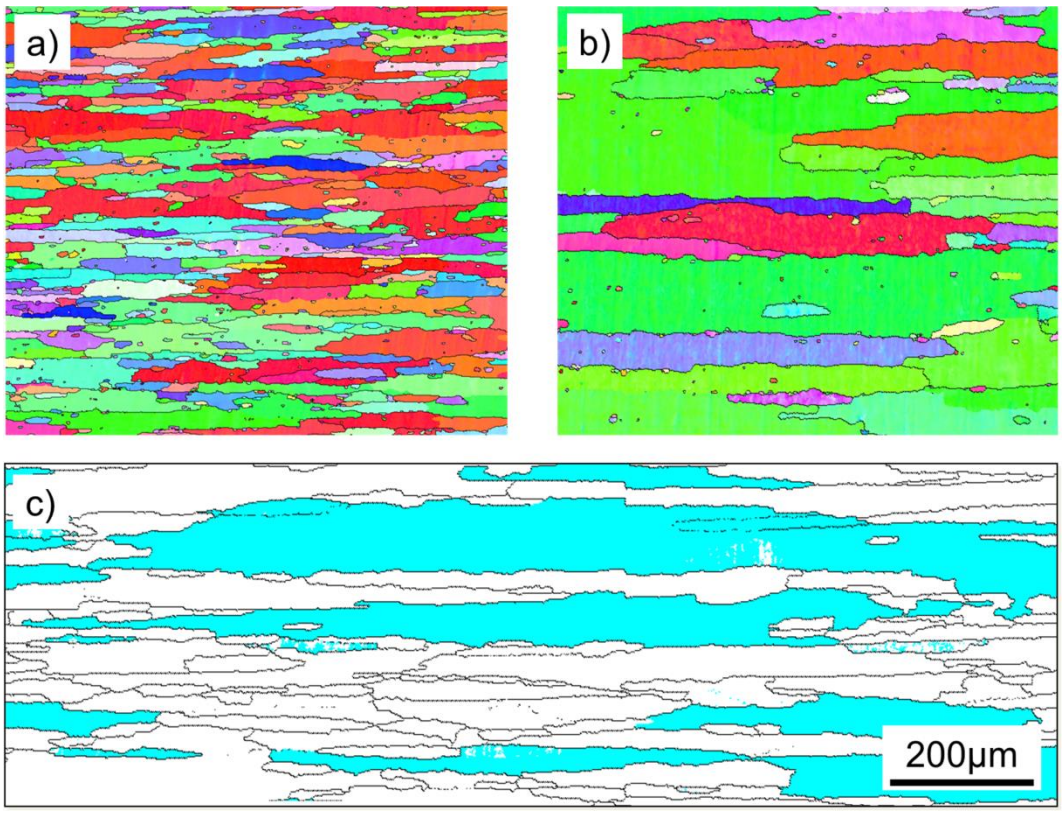

Fig.11 EBSD maps (TSL software) showing the recrystallized microstructure after annealing of the deformed samples at 325°C for 10^5s by three different temperature-time paths. a) IPF maps, isothermal annealing at 325°C for 10^5s; b) IPF map, slow annealing to 325°C for 10^5s; c) The same condition as b), but with large area and the P-orientations are coloured in light blue.

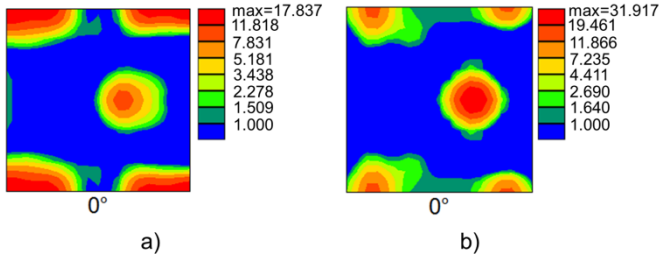

Fig.12 ODF maps (TSL software) showing the recrystallization textures after annealing of the deformed samples at 325°C for 10^5s by two different temperature-time paths. a) Isothermal annealing at 325°C for 5s; b) Slow annealing at 325°C for 10^5s.

Table 5 The volume fraction of typical recrystallization texture components after annealing of the deformed samples at 325°C for 10^5s by two different temperature-time paths, together with maximum texture intensities in ODF and the average recrystallized grain size

	Cube (%)	ND-Cube (%)	P (%)	Max. texture intensity (times random, R)	Average gain size (μm)
Isothermal annealing	13.4	22.9	24.7	17.9	103.9
Slow annealing	1.6	19.2	45.7	31.9	199.6

It appears that P-texture being the strongest texture component only takes place under annealing conditions where type II *and* type III dispersoids are present. This agrees well with existing literature [5, 13], where type II and type III dispersoids were collectively termed as "concurrent precipitation". *With the involvement of these dispersoid populations*, low annealing temperatures and slow annealing promote a stronger P-texture, together with a coarse elongated grain structure. This indicates that dispersoids precipitated out during annealing after deformation play an important role.

Most studies have been focused on the **combined** effect of dispersoids occurring *concurrently* with recrystallization (type III) and dispersoids precipitated out *prior to* recrystallization (type II). Since both populations of dispersoids tend to locate at grain/subgrain boundaries which are aligned along the RD direction and thus give stronger pinning effect along the ND direction, it is actually unclear whether the dispersoids precipitated before recrystallization (type II) also lead to the formation of a strong P-texture. In a previous work [15], the effect of this type of dispersoids was investigated, but the P-texture was not the dominant texture component. By using the two-step and three-step annealing, the effect of type II dispersoids on the development of P-texture is investigated more closely in this work.

When the samples were annealed with three different heating paths to 500°C, as shown in Fig.4a-c, recrystallization completed within 5s at 500°C and concurrent precipitation is insignificant. The two-step and three-step annealed samples, for which dispersoids precipitated along grain/subgrain boundaries (type II) before the final annealing step, exhibit relatively larger volume fractions of the P-texture component (see Table 2), indicating that this type of dispersoids also contribute to a stronger P-texture. It is noted that the volume fractions of P-texture are only around 12% (see Table 2), which is indeed not very high. Actually, the intensities of P-texture after two- and three-step annealing were always lower than their corresponding slow-annealed counterparts even at low annealing temperatures, see Tables 3 and 4. All these observations confirm that dispersoids of type II do contribute to a stronger P-texture, but to a much less extent than type III dispersoids. Type II dispersoids were deemed as more efficient in promoting a stronger P-texture during annealing of a cold rolled (90% reduction) AA 3004 alloy at 510°C in Ref [10] considering two initial states, one as-received variant and the other with additional heat treatment before cold rolling to generate densely distributed precipitates (type II). This conclusion, however, was based on an unjustified comparison. The reason is that recrystallization could complete in a very short time at 510°C, i.e., no significant concurrent precipitation was actually involved in the as-received material during recrystallization.

The strong P-texture must be closely related to type III dispersoids. The isothermal annealing step at 300°C for 10^4s obviously leads to significant precipitation before recrystallization, as reflected by the increase of EC (1.8 m/Ωmm^2) shown in Table 1 and discussed in Section 3.1. However, this step also decreases the precipitation potential during recrystallization, i.e., concurrent precipitation, although remaining supersaturated Mn can still precipitate during the final annealing step [2]. The same reasoning also applies to the three-step annealed sample which

contains some additional finer dispersoids precipitated out during the first annealing step where the sample was heated at 50°C/h to 300°C (Fig.3b) and the increase in EC value was thus even higher (2.1 m/Ωmm^2). For the slowly annealed cases, when the samples were heated at 50°C/h, recrystallization starts at 325°C where the increased EC (1.6 m/Ωmm^2) was the smallest, so there will be a *higher potential* for concurrent precipitation (type III) during recrystallization.

The effect of the amount of deformation before annealing on the formation of P-texture is not discussed in this work. It is well accepted, however, that large deformations promote a stronger P-texture [5, 13, 26, 31, 35]. When all the other affecting factors are the same, the increase of deformation favours nucleation by particle stimulated nucleation (PSN) since the critical particle size for PSN decreases with deformation [36], which then contribute to the formation of P-grains as discussed in Section 4.1. A strong P-texture was also observed during isothermal annealing at 300°C of a commercial purity aluminium (i.e., weak concurrent precipitation) cold rolled to ultrahigh strain of $\varepsilon_{VM} = 5.7$ [37]. It seems large cold deformation can compensate, to some extent, the weaker concurrent precipitation to promote the growth advantage of P-grains. However, no clear elongated P-grains like those shown in Fig.11c were observed, even though P-grains were larger than grains with other orientations [37]. For particle-containing AA3xxx alloys, large cold deformations also promote more heterogeneous recrystallization sites like grain boundaries, but dispersoids are preferentially precipitated out at these sites [5, 6] during annealing at low temperatures, nucleation from these sites is thus mainly suppressed. Based on the same reasoning, it is expected that a larger average size of the constituent particles strengthens the P-texture, even though this aspect has not been systematically investigated so far.

4.4 Formation mechanism of a strong P texture

It follows from Section 4.2 that dispersoids of type III is essential for the formation of a strong P-texture, let us now discuss how they favours strong P-texture.

According to the classic Zener pinning equation,

$$P_Z = \frac{3\gamma_{GB} f_V}{2r} \tag{1}$$

where γ_{GB} is the grain boundary energy, r and f_V are the average size and volume fraction of the dispersoids, respectively. If P-orientations have a close to 40°<111> special orientation relationship with the deformed matrix, concurrent precipitation is less favoured at these special boundaries due to their more ordered structure (and thus lower energy [30]). The moving boundaries of P-oriented grains suffer less pinning effect due to the smaller volume fraction of dispersoids. Similar effects have also been documented for other materials, e.g., particle containing copper single crystals [38], Fe-Cr alloys [39] and Fe-Si transformer steels [40, 41].

Meanwhile, their smaller grain boundary energy also leads to less pinning pressure (P_Z), since P_Z is directly proportional to the grain boundary energy (γ_{GB}) according to eq. (1). It implies that these special grain boundaries will be less affected by encountered dispersoids during their migration, including type I dispersoids and precipitated dispersoids that already have detached from their 'host' grain boundaries. This makes the growth of P-orientation even more favourable. Is there anything else that also contribute to a strong P-texture?

One important aspect to check is the possible nucleation advantage of P-grains. However, at the beginning of the recrystallization process, this nucleation advantage for P-grains is not really significant even at low annealing temperatures where strong P-texture prevails, the reason being that the nucleation in general is quite weak at low annealing temperatures and other orientations

can still be nucleated through PSN. An example of early recrystallization at low annealing temperature during slow annealing is shown in Fig.13, a few recrystallized grains (pointed out by black arrows) with other orientations are present when the sample was slowly annealed at 50°C/h to 325°C. P-oriented grains with a small size, as indicated by blue arrows, can indeed be seen but the number density is not high. This small number of P-grains makes their quantification difficult, extremely large EBSD maps are needed to generate statistically reliable data. However, it is reasonable to state that any significant nucleation advantage of P-grain does not emerge from the available data.

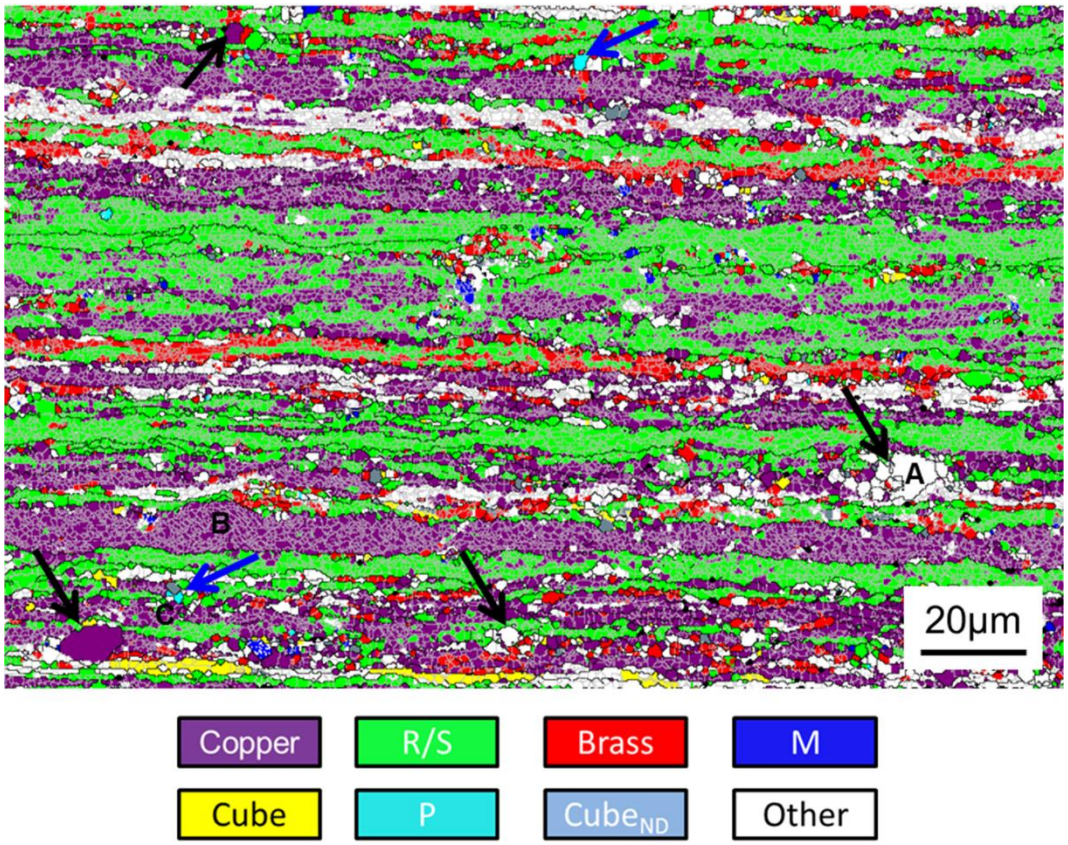

Fig.13 The grain orientation map (HKL software) showing the grain structure after annealing of a deformed sample at 50°C/h to 325°C without any additional holding time. Black lines represent grain boundary with misorientation $\theta>15°$, low angle grain boundaries in grey with $1°<\theta<15°$ are also plot to represent the deformed matrix. Grains labelled by letter A, B and C will be further discussed.

There is no clear evidence of any nucleation at old grain boundaries (e.g., see the boundaries of the elongated Copper grain labelled by letter B) and other heterogeneous nucleation sites such as deformation bands, shear bands etc. Nucleation at these nucleation sites is mainly suppressed because they are also favourable sites for precipitation [5, 6]. PSN nuclei with other than the P-orientation can be formed, as shown in Fig.14a (area near grain A in Fig.13), but will suffer from concurrent precipitation during their subsequent growth and thus only experience a limited growth rate, and will thus not become dominant texture components. The grain labelled C in Fig.13 (pointed out by the blue arrow near the bottom left corner), identified as a P-oriented grain is indeed located around a large particle, as shown in Fig.14b.

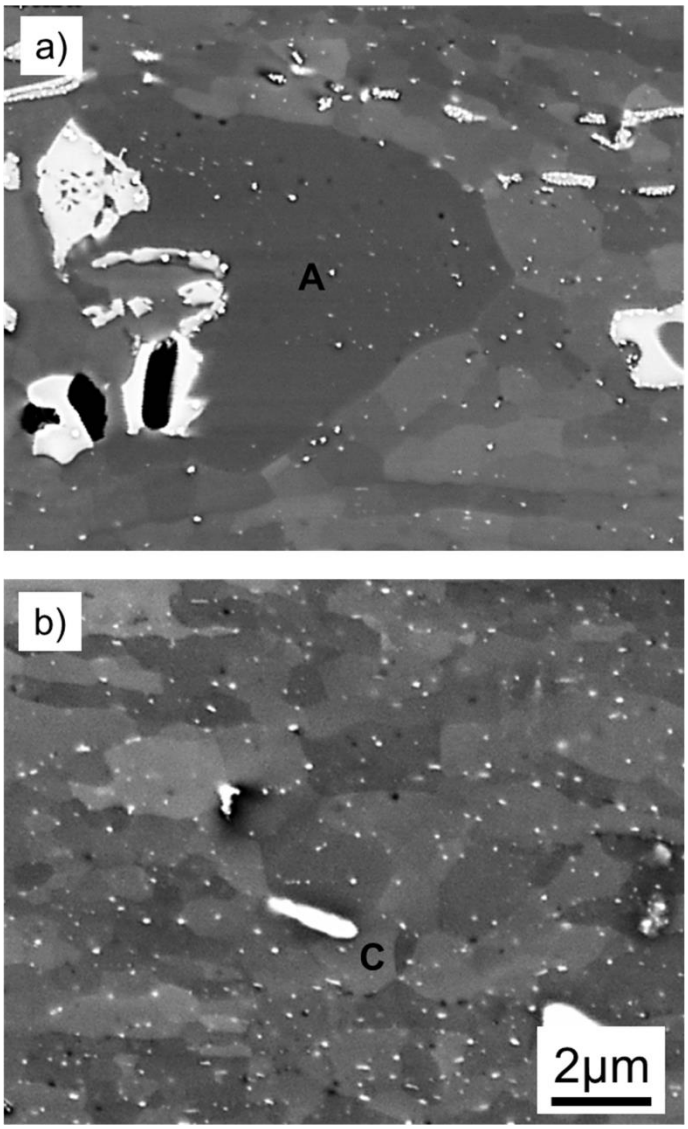

Fig.14 BSE images showing the particles and recrystallized grains after annealing of a deformed sample at 50°C/h to 325°C without any additional holding time.

a) the PSN grain A, as shown in Fig.13; b) the small P-grain, as labelled C in Fig.13.

When precipitation occurs concurrently with recrystallization, the average size of P oriented grains *after recrystallization* is larger than the average size of all orientations [13, 16], which is a clear evidence that P-oriented grains grow faster than other orientations since there is no size advantage in the nucleation stage. A fast growing P-grain, with size a few times larger than its

surrounding grains, is shown in Fig.15 after slow heating to 335°C. This significant size advantage of P-grains actually makes it unnecessary for quantitative comparison of the grain sizes with other orientations. Low angle grain boundaries with misorientation θ>5° are also plotted as grey lines, which makes it possible to distinguish recrystallized grains from deformed ones. Here, fast growing segments of P-oriented grains form protrusions (as pointed out by black arrows), while segments with ordinary migration rate lead to several retrusions (as pointed out by red arrows). The boundary curvatures resulting from the retrusions provide an extra driving force for growth [42-44] to catch up with, to some extent, the growth of the part with fast migration rate. This behavior may explain why only a limited number of retrusions are observed for the P-grains in the fully recrystallized state during slow annealing at low temperatures, as shown in Fig.11c. Since the P-grain grows much faster than others, small grains of other orientations are encircled by the P-grain, shown as small islands within the P-grain in Fig.15.

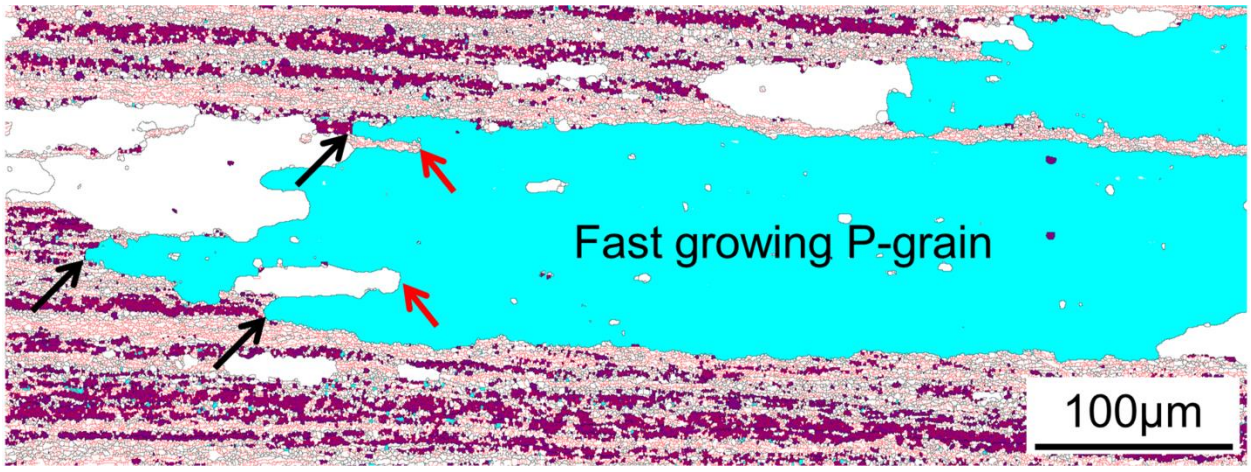

Fig.15 The growing P-grain with protrusions and retrusions (HKL software), the sample was cold deformed to ε=3 and then annealed at 50°C/h to 335°C without any holding time. To avoid as much overlap between different texture component as possible, only P- and Cu-grain with 7° and 10° deviation from the ideal orientations are colored, in aqua and purple, respectively. LAGBs are shown as red lines.

Besides the effect of morphology, it is also clearly noted that the fast growing sections (e.g. sections pointed out by black arrows in Fig.15) of the P-grain always grow preferentially along the deformed matrix with Cu orientation. One small area containing both fast and slow growing sections of the P-grain in Fig.15 is enlarged in Fig.16a. It has been suggested, both by Nes et al [5, 8] and Schäfer and Gottstein [14], that P-oriented grains exhibit a close to 40°<111> orientation relationship with respect to the Cu-orientation , but direct experimental evidence has not been provided due to the difficulties mentioned in section 4.2. A plot of the {111} pole figure of the fast growing P-grain and the deformed Cu-grain F indeed shows that these two grains have a close to 38°<111> orientation (~32-39°<111> due to the points scattering within the deformed Cu-grain, see Fig.16b), this thus confirms, for the first time, the hypothesis made in previous Refs [5, 8, 14, 31]. Similar results were obtained between the P-grain and deformed matrix just in front of the fast growing sections (see Fig.15) which all belonged to the Cu-orientation. The retrusion close to letter B was formed due to unfavorable orientation relationships between the growing P-grain and the deformed matrix, i.e., far away from 40°<111> orientation relationship (~53-57°<144>), as illustrated in Fig.16c. Also of high interest is why the P-grain does not grow equally along the ND direction, unfavorable orientation relationship with the neighboring deformed matrix is certainly one of the reasons. Another aspect that we have not yet discussed with respect to the fast growing P-grain is the effect of dispersoids, which will be analyzed below.

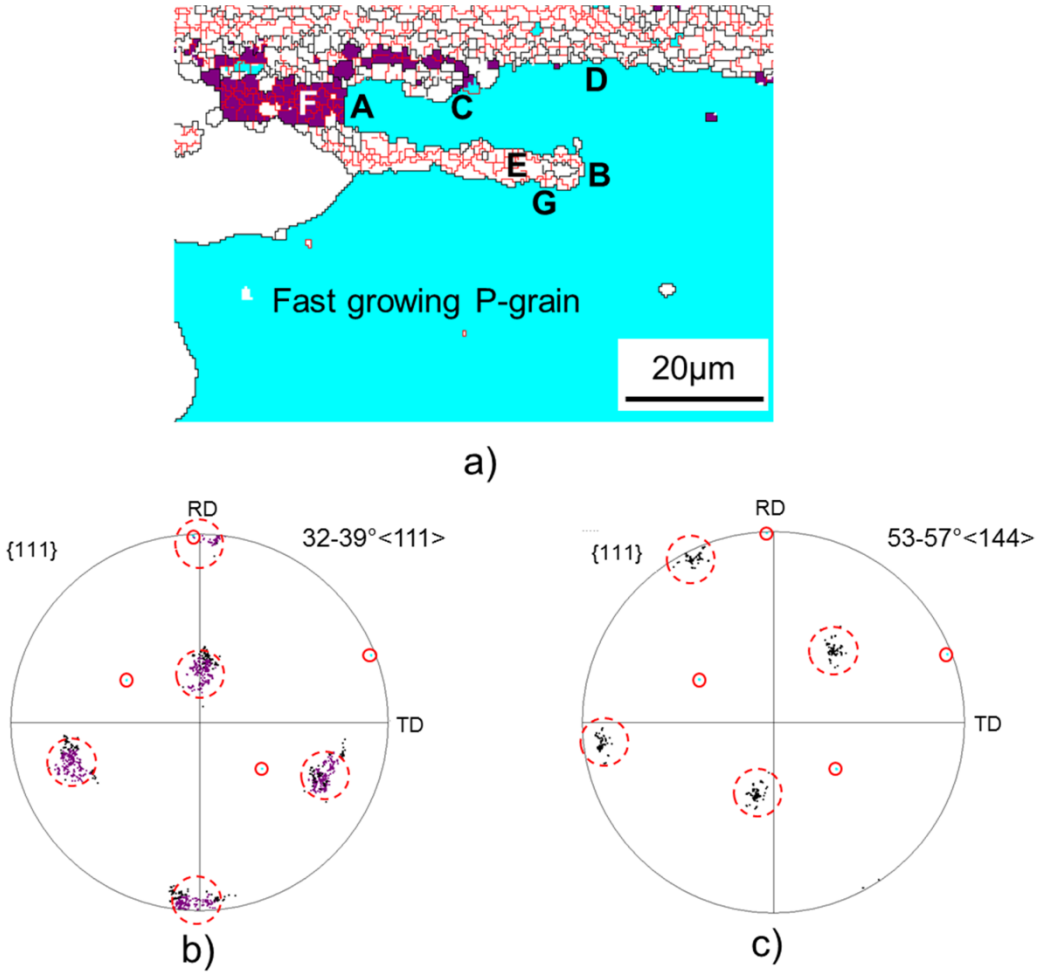

Fig. 16 The fast growing sections of P-grain (in aqua) and its surrounding deformation matrix (HKL software) where Cu-grains are colored in purple, cold deformed sample to ε=3 and then annealed at 50°C/h to 335°C without any holding time. a) Orientation map; b) {111} pole figure showing the positions of P-grain (encircled by red line) *with* close to 38°<111> relationship with its neighboring Cu-grain F (encircled by broken red line); c) {111} pole figure showing the positions of P-grains *without* 38°<111> relationship with its neighboring grain E (encircled by broken red line) ; The black points are pixels that do not satisfy the strict orientation definitions of P- and Cu-grain (7° and 10° deviation from the ideal orientations to reduce the scattering of deformed grains in the pole figure).

The interaction between the growing P-grain and second-phase particles is further examined with BSE images in Fig. 17, corresponding to selected areas of Fig.16a. It can be seen that there are indeed no clear small precipitates on the grain boundaries between the fast growing section A

and deformed matrix F (Fig.17 a). These grain boundaries have successfully broken away from a number of dispersoids, including larger type I dispersoids, smaller type II dispersoids, and perhaps a very small number, if any, of type III dispersoids. The grain boundary shown in Fig. 17a is almost parallel to the ND direction, quite different from the jagged boundaries typically observed when they are strongly affected by dispersoids [45]. This is by no means conclusive, but it clearly indicates that the boundary is indeed not very much affected by dispersoids.

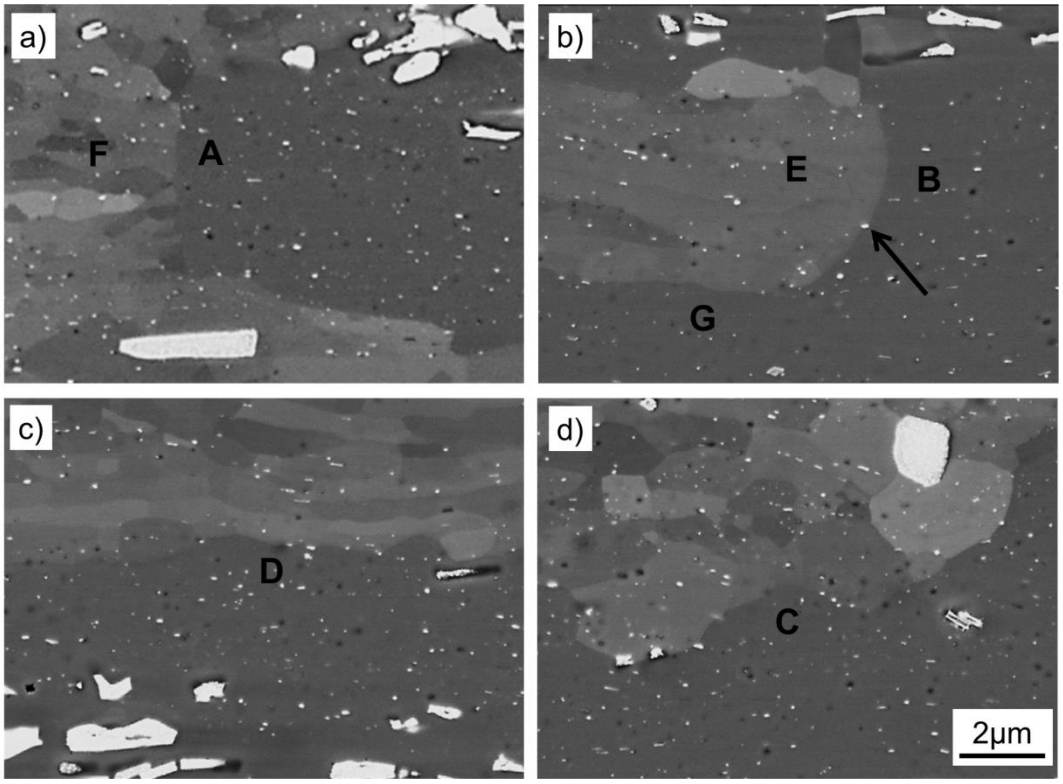

Fig. 17 The interaction between fast growing P-grain and second-phase particles, the sample was cold deformed to ε=3 and then annealed at 50°C/h to 335°C without any holding time. The four different areas are taken from Fig.15a. a) Fast growing section A; b) Slow growing section B; c) Stationary boundary D; d) Small recrystallized non-P-grains pinned by dispersoids.

Knowing that the fast moving grain boundaries between P-grains and neighboring Cu-grains are indeed not significantly affected by dispersoids, it is also important to see how the boundaries

between P-grain/other orientations, as well as grain boundaries of other orientations react to dispersoids. For the slowly growing section B, the dispersoid (pointed out by a black arrow) on the grain boundary with the deformed matrix E is likely to be of type I due to its relatively large size. A smooth grain boundary, even though curved, is also observed here. This implies that the slow migration here is not due to particle pinning, it is mainly due to an unfavourable orientation relationship with the deformation matrix (see Fig.16c), i.e., it is a variant inhibition [46] or an orientation pinning effect [47]. The larger subgrain size (L_{RD} ~5μm, L_{ND} ~1μm) in the deformation matrix E, as compared to that in the deformed matrix F (L_{RD} ~2μm, L_{ND} ~1μm) in Fig.17a, which indicates a lower stored energy in that region, might be another reason for the slow migration. The boundary curvature provides additional driving force for the migration of the moving boundary close to B. Without this extra driving force, the boundary near G is almost stationary (see Fig.17b), a global view is shown in Fig.16a. Another area around D in Fig. 16a containing the grain boundary between a P-oriented grain and deformed matrix, is also enlarged and shown in Fig.17c. This non-special boundary is decorated with quite a few dispersoids. It is an ordinary high angle grain boundary possibly subjected to orientation pinning, thus mainly stationary and as such a preferential site for concurrent precipitation. There are a few recrystallized grains of orientations other than the P orientation in the area close to C in Fig.16a, these few grains are strongly pinned by dispersoids of different sizes (as shown in Fig.17d), they will thus to a limited degree contribute to the final recrystallization texture due to their small sizes. If these grains with other orientation were not so strongly pinned by concurrent precipitation, they could keep growing and consume the deformation matrix, including those with Cu-orientation, making the protrusions and retrusions less evident. This is probably the case

when the deformed samples are annealed using other temperature-time paths which involve less concurrent precipitation, i.e., isothermal annealing, two- and three-step annealing.

From the results presented in this study, together with the previous investigations on the same type of alloys [4, 13, 15, 16, 48], it is now possible to explain the formation of a strong P-texture for all known cases by considering these combined factors: 1) A large deformation to promote formation of the P-orientation by PSN; 2) the special orientation relationship of P-oriented grains with respect to the deformed matrix, thus favouring the growth of P-oriented grains due to their boundaries' high mobility and reduced pinning pressure; 3) P-grains enjoy an additional driving force from curvature due to their uneven migration rate (see Fig.14) caused by orientation pinning; 4) low recrystallization temperature leads to reduced recrystallization kinetics and significant *concurrent precipitation*. Since not all P-oriented grains fulfill these combined factors, small P-grains still exist during and after recrystallization, see Fig.15 and Fig.11c, respectively. A strong P-texture condition is mainly dominated by coarse elongated P-grains that meet all the conditions mentioned above. The dispersoids precipitated before the onset of recrystallization during step-annealing (before the final annealing step) do locate at grain/subgrain boundaries, and they act to suppress the nucleation of recrystallization, which yields recrystallized grains usually larger than their isothermally annealed counterparts. Since P-oriented grains are less affected by dispersoids during their growth, as already discussed at the beginning of this section, the P-component is always the strongest texture component after step-annealing. However, during subsequent final annealing steps, there will be less potential for concurrent precipitation, which is required to form coarser elongated P-grains leading to a stronger P-texture. Annealing of samples with a higher supersaturation level of Mn during slow heating will increase the recrystallization temperature due to stronger concurrent precipitation [4]. If this recrystallization

temperature is high enough to activate “all” nucleation sites for recrystallization, the higher solute level of Mn will not necessarily contribute to a strong P-texture, which was documented in Ref [4].

5. Conclusions

In this study, a cold-rolled model AA3xxx alloy was annealed with four different temperature-time paths after cold rolling. The effect of different populations of dispersoids on the subsequent recrystallization behaviour of the deformed material was investigated. The following conclusions are reached:

- As compared to isothermal annealing, annealing with more elaborate heating/annealing schedules all lead to an increased strength of the P-texture component and decreased intensities of both Cube and ND-rotated Cube texture components.
- The increase of P-texture strength and average grain size is most significant when recrystallization occurs concurrently with precipitation. The strength of the ND-rotated cube texture component is then much weaker than that of the P-texture component.
- When concurrent precipitation (type III disppersoids) is limited, due to fast recrystallization kinetics and/or lack of precipitation, the intensity of P-texture and the extent of coarse elongated grain structure are reduced, even in the presence of dispersoids preferentially located at grain/subgrain boundaries.
- The strong P-texture mainly comes from the *growth advantage* of P-grains during slow annealing where strong concurrent precipitation occurs, the contribution from its *nucleation advantage* is not evidenced, at least in the investigated alloy and conditions. The growth advantage of P-grains can be explained by their low grain boundary energy

combined with fast migration rate, and less pinning effect from different types of dispersoids, as well as by the additional driving force from the curvature resulted from variable migration rate of the moving boundaries.

- Precipitates which form before recrystallization (Type II) do promote coarser grain structure and stronger P-texture, but the fact that they lower the concurrent precipitation potential during subsequent recrystallization, which is a key factor for the growth advantage of P-orientations, is predominant. This is why they are less effective in producing the elongated coarse grain structure and strong P-texture, as compared to type III dispersoids.

Acknowledgements

This research work has been supported by the KMB project (193179/I40) in Norway. KH and REL acknowledge the financial support from PX Group.

Reference

[1] Y.J. Li, L. Arnberg, Quantitative study in the precipitation behavior of dispersoids in DC-cast AA3003 alloy during heating and homogenization, Acta Mater. 51 (2003) 3415–3428

[2] K. Huang, N. Wang, Y.J. Li, K.Marthinsen, The influence of microchemistry on the softening behaviour of two cold-rollled Al-Mn-Fe-Si alloys, Mater.Sci.Eng.A 601 (2014) 86-96

[3] H. Alborn, E. Hornbogen, U. Köster, Recrystallisation mechanism and annealing texture in aluminium-copper alloys, J. Mater. Sci 4(1969)944-950

[4] K. Huang, O. Engler, Y.J. Li, K. Marthinsen, Evolution in microstructure and properties during non-isothermal annealing of a cold-rolled Al–Mn–Fe–Si alloy with different microchemistry states, Mater.Sci.Eng.A 628(2015) 216-229

[5] S. Tangen, K. Sjølstad, T. Furu, E. Nes, Effect of concurrent precipitation on recrystallization and evolution of the p-texture component in a commercial Al-Mn alloy, Metall. Mater.Trans. A 41A (2010) 2970-2983

[6] M. Somerday, F.J. Humphreys, Recrystallization behavior of supersaturated Al-Mn alloys, Mater.Sci.Technol 19 (2003) 20-29

[7] K. Huang, R.E. Logé and K. Marthinsen, On the sluggish recrystallization of a cold–rolled Al–Mn–Fe–Si alloy, J. Mater. Sci. 51(2016) 1632-1643

[8] O. Daaland, E. Nes, Recrystallization texture development in commercial Al–Mn–Mg alloys. Acta Mater. 44(1996)1413-1435

[9] W.C. Liu, J.G. Morris, Evolution of recrystallization and recrystallization texture in continuous-cast AA 3015 aluminum, Metall. Mater.Trans. A 36 (2005) 2829-2848

[10] Q. Zeng, X. Wen, T. Zhai, Effect of precipitates on the development of P orientation {011}<566> in a recrystallized continuous cast AA3004 aluminium alloy after cold rolling. Metall. Mater. Trans A, 40A(2009) 2488-2497

[11] W.C. Liu, Z. Li, C.S. Man, Effect of heating rate on the microstructure and texture of continuous cast AA 3105 aluminum alloy, Mater.Sci.Eng. A 478 (2008) 173-180

[12] W.C. Liu, J.G. Morris, Recrystallization textures of the M{113}<110> and P{011}<455> orientations in a supersaturated Al–Mn alloy, Scr. Mater. 56 (2007) 217-220

[13] K. Huang, Y.J. Li, K. Marthinsen, Factors affecting the strength of P {011}< 566>-texture after annealing of a cold-rolled Al–Mn–Fe–Si alloy, J. Mater. Sci 50(2015) 5091-5103

[14] C. Schäfer, G. Gottstein, The origin and development of the P{011}<111> orientation during recrystallization of particle-containing Alloys, Int. J. Mater. Res, 102 (2011) 1106-1114.

[15] K. Huang, Y.J. Li, K. Marthinsen, Effect of heterogeneously distributed pre-existing dispersoids on the recrystallization behavior of a cold-rolled Al–Mn–Fe–Si alloy, Mater. Charact 102 (2015) 92-97

[16] Q.L. Zhao, K. Huang, Y.J. Li, K. Marthinsen, Orientation preference of recrystallization in supersaturated aluminum alloys influenced by concurrent precipitation, Metall. Mater. Trans A (2016) 1378-1388

[17] A. Miroux, Z. J. Lok, S. Van der Zwaag, Recrystallisation and concurrent precipitation in hot rolled AA3103, Mater. Sci. Forum, 467-470(2004)393-398

[18] C. Schäfer, V. Mohles, G. Gottstein, Modeling of non-isothermal annealing: Interaction of recrystallization, recovery, and precipitation, Acta Mater. 59 (2011) 6574-6587

[19] J.J. Sidor, K. Decroos, R. H. Petrov, L. A. I. Kestens, Evolution of recrystallization textures in particle containing Al alloys after various rolling, Inter J. Plasticity 66(2015) 119-137

[20] Y.J. Li, L. Arnberg, Evolution of eutectic intermetallic particles in DC-cast AA3003 alloy during heating and homogenization, Mater. Sci. Eng. A 347 (2003) 130–135

[21] R. Ørsund, E. Nes, Effect of particles on recrystallization textures in aluminium–manganese alloys, Scr. Metall. 22(1988) 665-669.

[22] Y.J.M. Bréchet, H.S. Zurob, R. Christopher, On the effect of pre-recovery on subsequent recrystallization, Int J Mater Res. 100 (2009) 1446-1448.

[23] B. Decreus, H.S. Zurob, Y.J.M. Bréchet, Effect of low-temperature recovery treatments on subsequent recrystallization in Al-2.5%Mg, Mater Sci Forum. 550(2007) 381-386.

[24] L. Huang, G. Huang, L. Gao, X. Wu, Z. Jia, M. Xia, Q. Liu, Influence of pre-recovery on the subsequent recrystallization and mechanical properties of a twin-roll cast Al-Mn alloy, Mater Sci Eng A 682(2017) 63-72

[25] O. Engler, Nucleation and growth during recrystallization of aluminium alloys investigated by local texture analysis, Mater. Sci. Tech. 12 (1996) 859-872.

[26] O.V. Mishin, A. Godfrey, D. Juul Jensen, N.Hansen, Recovery and recrystallization in commercial purity aluminium cold rolled to an ultrahigh strain, Acta Mater. 61 (2013) 5354-5364

[27] O. Engler, P. Yang, X.W. Kong, On the formation of recrystallization textures in binary Al-1.3% Mn investigated by means of local texture analysis, Acta Mater. 44 (1996) 3349-3369

[28] J.-H. Ryu, D.N. Lee, The effect of precipitation on the evolution of recrystallization texture in AA8011 aluminum alloy sheet, Mater. Sci. Eng. A 336 (2002) 225-232

[29] C. Schäfer, J. Song, G. Gottstein, Modeling of texture evolution in the deformation zone of second-phase particles, Acta Mater. 57 (2009) 1026-1034

[30] J.J. Sidor, R.H. Petrov, L.A.I.Kestens, Modeling the crystallographic texture changes in aluminum alloys during recrystallization, Acta Mater. 59(2011) 5735-5748

[31] J. Jung, J.I. Yoon, D.N. Lee, H.S. Kim, Numerical analysis on the formation of P-orientation near coarse precipitates in FCC crystals during recrystallization. Acta Mater. 131(2017)363-372

[32] F.J. Humphreys, M. Hatherly, Recrystalliaztion and related Annealing Phenomena, Second ED., Elsevier, Oxford, 2004

[33] P.A. Beck, P.R. Sperry, H. Hu, The orientation dependence of the rate of grain boundary migration, J. Appl. Phys. 21(1950) 420-425

[34] G.H. Fan, Y.B. Zhang, J.H. Driver, D. Juul Jensen, Oriented growth during recrystallization revisited in three dimensions, Scr. Mater. 72-73(2014) 9-12

[35] W.C. Liu, H. Yuan, M. J. Huang, Effect of rolling reduction on the P{011}< 455> recrystallization texture in a supersaturated Al–Mn–Mg alloy, Metall. Mater. Trans A 40A (2009) 2794-2797

[36] F.J. Humphreys, The nucleation of recrystallization at second phase particles in deformed aluminium, Acta. Metall 25(1977) 1323-1344

[37] O.V. Mishin, D. Juul Jensen, N. Hansen, Evolution of microstructure and texture during annealing of aluminium AA1050 cold rolled to high and ultrahigh strains, Metall. Mater. Trans A 41 (2010) 2936-2948

[38] F.J. Humphreys, M.G. Ardakani, Grain boundary migration and Zener pinning in particle-containing copper crystals, Acta Mater. 44(1996)2717–2727.

[39] D. Raabe, K. Lücke, Selective particle drag during primary recrystallization of Fe-Cr alloys, Scr. Matell. 26(1992)19–24.

[40] Y. Ushigami, K. Kawasaki, T. Nakazama T, Y. Suga, J. Harase, N. Takahashi. Dynamic observation of the growth of secondary recrystallized grains of Fe-35 Si alloy utilizing synchrotron X-Ray topography, Mater.Sci. Forum 157-162 (1994) 1081-1086–323.

[41] H. Homma, B. Hutchinson. Orientation dependence of secondary recrystallisation in silicon-iron, Acta Mater 51(2003) 3795-3805

[42] Y.B. Zhang, A. Godfrey, D. Juul Jensen, Local boundary migration during recrystallization in pure aluminium, Scr. Mater. 64 (2011) 331-334

[43] N. Moelans, A. Godfrey, Y.B. Zhang, D. Juul Jensen, Phase-field simulation study of the migration of recrystallization boundaries, Phys. Rev. B 88 (2013) 054103

[44] F.X. Lin, Y.B. Zhang, W. Pantleon, D. Juul Jensen, Supercube grains leading to a strong cube texture and a broad grain size distribution after recrystallization, Philos. Mag. 95(2015) 2427-2449

[45] F.J. Humphreys, J.W. Martin, The effect of dispersed silica particles on the recovery and recrystallization of deformed copper crystals, Acta Mater. 14(1966)775-781

[46] R.D. Doherty, Recrystallization and texture. Prog Mater Sci. 42(1997) 39-58

[47] D. Juul Jensen, Growth rates and misorientation relationships between growing nuclei/grains and the surrounding deformed matrix during recrystallization. Acta Metall. Mater. 43(1995) 4117-4129

[48] K. Huang, K. Marthinsen, The effect of heating rate on the softening behaviour of a deformed Al–Mn alloy with strong and weak concurrent precipitation, Mater. Charact. 110(2015) 215-221